





## Rarest rainfall events will see the greatest relative increase in magnitude under future climate change

Gaby Joanne Gründemann <sup>1,2</sup>✉, Nick van de Giesen <sup>1</sup>, Lukas Brunner <sup>3,4</sup> & Ruud van der Ent <sup>1</sup>

Future rainfall extremes are projected to increase with global warming according to theory and climate models, but common (annual) and rare (decennial or centennial) extremes could be affected differently. Here, using 25 models from the Coupled Model Intercomparison Project Phase 6 driven by a range of plausible scenarios of future greenhouse gas emissions, we show that the rarer the event, the more likely it is to increase in a future climate. By the end of this century, daily land rainfall extremes could increase in magnitude between 10.5% and 28.2% for annual events, and between 13.5% and 38.3% for centennial events, for low and high emission scenarios respectively. The results are consistent across models though with regional variation, but the underlying mechanisms remain to be determined.

<sup>1</sup>Department of Water Management, Faculty of Civil Engineering and Geoscience, Delft University of Technology, Delft, Netherlands. <sup>2</sup>Centre for Hydrology, University of Saskatchewan, Canmore, AB, Canada. <sup>3</sup>Institute for Atmospheric and Climate Science, ETH Zurich, Zurich, Switzerland. <sup>4</sup>Present address: Department of Meteorology and Geophysics, University of Vienna, Vienna, Austria. ✉email: [g.j.gruendemann@tudelft.nl](mailto:g.j.gruendemann@tudelft.nl)

Global warming will result in an intensification of the water cycle<sup>1</sup>. An increase in rainfall extremes is already observed in many regions in the world<sup>2–6</sup>, and research shows that extremes will increase in the future depending on the emission scenario<sup>7–11</sup>. Global climate models (GCMs) are the only available tools to study future daily rainfall extremes on the global domain, but come with limitations. A large limitation is that GCMs do not resolve convective processes, which are important drivers of extreme precipitation<sup>12,13</sup>. Recent research demonstrates that GCMs included in the Coupled Model Inter-comparison Project Phase 6 (CMIP6)<sup>14</sup> have decent skill in modelling extreme rainfall in comparison to observations<sup>15</sup>. Yet, when interested in absolute magnitudes or specific locations, a careful selection of models based on observations or advanced bias correction approaches are necessary<sup>16–18</sup>, but these are less relevant when studying relative changes over time.

Studies investigating the simulation of rainfall extremes in global climate models typically focus on one of two types of extremes: (1) common and (2) rare. Climate indices focusing on “common” extremes typically have probabilistic return times of a year or less. Examples of such indices include annual maxima<sup>5,19</sup>, a percentile-based threshold, e.g. the 90th, 95th, 99th, or 99.9th percentile<sup>20–22</sup>, or indices like R20mm (the number of days per year in which precipitation depth exceeds 20 mm) as defined by “the expert team on climate change detection and indices”<sup>8,23,24</sup>. These indices are well-studied on global and regional domains, and many regions expect a substantial increase in such common extremes<sup>9,19,20,22,23,25</sup>. The second type of extremes are the “rare” ones with multi-year or multi-decade return time periods, which are important for infrastructure design<sup>10</sup>. In hydrology these are typically estimated based on extreme value theory (using a historical time series of the same location), but model-based (e.g.<sup>26,27</sup>) or spatial pooling-based approaches (e.g.<sup>28,29</sup>) also exist to increase the time series length. There are fewer studies on the effect of global warming on such rare extremes<sup>30–32</sup>, or on the differences in future changes between “common” to “rare” extremes<sup>15,27</sup>. The latter studies point to a possible larger relative increase of the rare extremes.

The scientific debate regarding the effect of global warming on rainfall extremes has not yet fully addressed this difference in the expected change for the common and rare extremes, and if that differs for different climatic regions across the world. Here, we investigate the spatiotemporal patterns of a range of common to rare extremes using a large ensemble of precipitation estimates from the GCMs included in CMIP6<sup>14</sup>.

We analyse the simulations of daily precipitation of 25 CMIP6 GCMs for both the historical late twentieth century period (1971–2000, referred to as “historical”) and the future late twenty-first century period (2071–2100, referred to as “future”) forced by four different scenarios (SSP1-2.6, SSP2-4.5, SSP3-7.0 and SSP5-8.5)<sup>33</sup>. To achieve robust multi-model ensemble statistics it is important to account for (a) model independence, i.e. the fact that some GCMs originate from similar development branches or share components and (b) model performance, i.e. the models’ ability to simulate historical climate<sup>34</sup>. Here we use the Climate model Weighting by Independence and Performance method<sup>35–39</sup> to weight models by both independence and performance (see “Methods” for details). The multi-model ensemble means shown in this manuscript are weighted using the described method, but we note that using unweighted estimates does not considerably affect the results and conclusions drawn in this study (see Supplementary Figs. S1–S3).

Extreme precipitation return levels ranging from common to rare were estimated using frequency and extreme value analyses (see “Methods”). We found the results to be largely independent of the statistical method, but here we mainly show the results

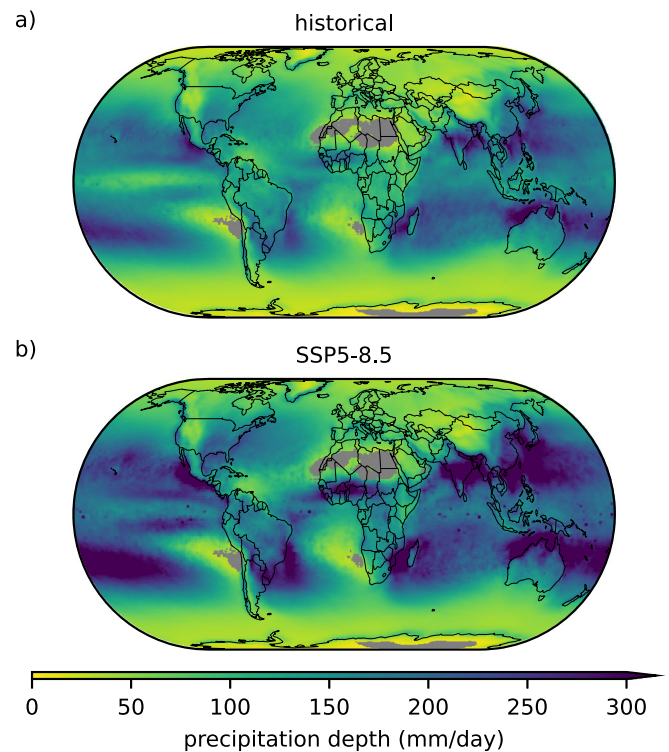


**Fig. 1 The 100-year return level of daily precipitation.** The 100-year return level of daily precipitation weighted mean across 25 CMIP6 models for **a** historical (1971–2000) and **b** SSP5-8.5 future (2071–2100) periods. The individual model results are shown in Supplementary Figs. S4 and S5. Dry areas (weighted mean of less than 3 events per year) are masked in grey.

obtained by using the metastatistical extreme value (MEV) distribution<sup>40,41</sup> as it produces the smoothest spatial patterns<sup>42,43</sup> and reduces uncertainty for the rarest extremes<sup>40</sup>.

This study is focused on relative changes in precipitation extremes in order to overcome the issues of systematic bias and different climate model resolutions. Moreover, relative changes allow for comparison between geographical regions with highly different precipitation amounts. As a reference for absolute values, we show the weighted mean precipitation depth for a precipitation event that would occur on average once every 100 years in Fig. 1 (see Supplementary Figs. S4 and S5 for the individual models). The highest model agreement is shown over the higher latitudes and arid regions, the lowest over the tropics, which most models have issues simulating correctly<sup>10,23,44</sup> (see Supplementary Fig. S6).

## Results

Future precipitation extremes for the climate scenarios are expected to increase in magnitude over land compared to historical extremes (Fig. 2 and Supplementary Figs. S7–9). This increase has high model agreement, irrespective of the climate scenario or how rare the extremes are. Regions with the largest magnitude increase in future extremes are mainly located in areas around and just north of the equator, stretching from the Equatorial Pacific Ocean, via northwest South America, through the Sahara and Western, Central and Eastern Africa, the Arabian Peninsula and Arabian Sea to South Asia and the Tibetan Plateau. There are some locations over the subtropical Atlantic and South Pacific oceans where extreme precipitation is expected to decrease in the future, though more so for the common return levels. This is in agreement with findings by Pfahl et al.<sup>45</sup>, who demonstrated that the dynamic contribution of daily precipitation over

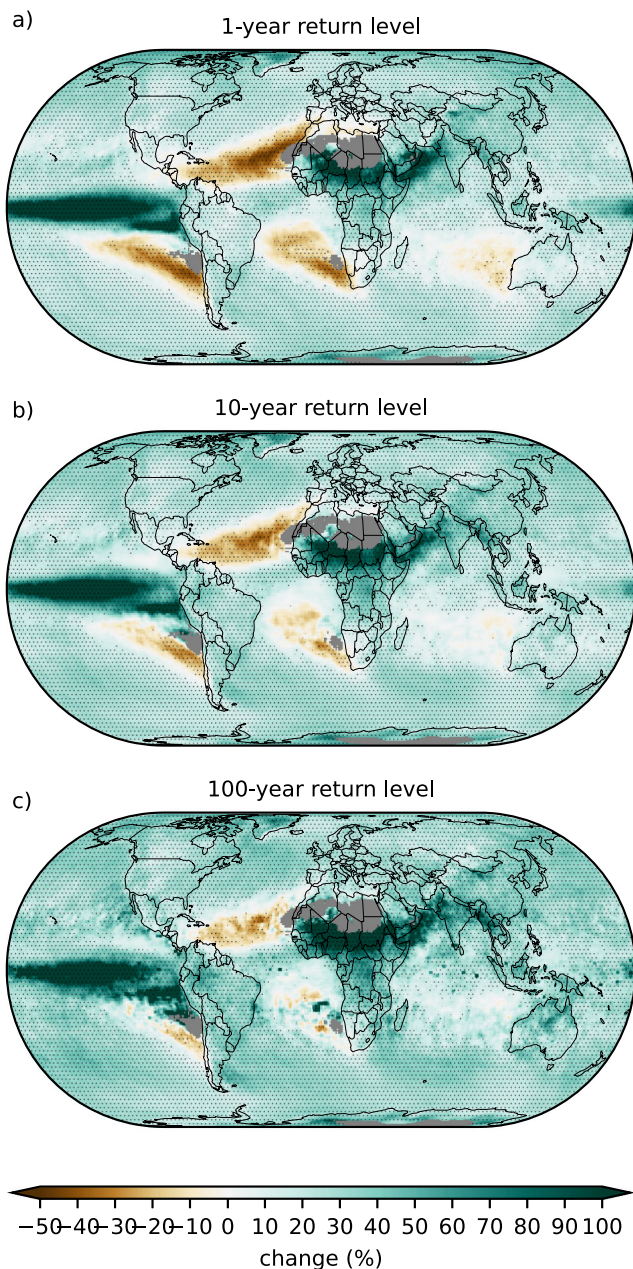


**Fig. 2 Relative change of future vs historical precipitation return levels.** Relative change of the **a** 1, **b** 10 and **c** 100-year return levels of daily precipitation expressed as weighted mean across 25 CMIP6 models for the SSP5-8.5 future period (2071–2100) with respect to the historical period (1971–2000) (Eq. (2)). Hatching is in the locations where >75% of the weighted models agree on the sign of the change. Dry areas (weighted mean of less than 3 events per year) are masked in grey.

subtropical oceans causes robust regional decreases in extreme precipitation. These regional patterns of increasing and decreasing precipitation extremes are similar to those of Li et al.<sup>15</sup>, their Fig. 5. Furthermore, the areas with the highest increases and lowest decreases overlap with the areas with the most positive and negative scaling with dew point temperature<sup>46</sup>, their Fig. 4.

The rarest precipitation extremes (i.e. the blue squares in Fig. 3) will increase more relative to the more common ones (i.e. the green triangles in Fig. 3). As expected, all individual models predict a global median magnitude increase in extreme precipitation for each of the four SSPs. However, the finding that this increase is relatively larger for rarer extremes is to the best of our

knowledge the novel part of the results. Technically, this implies that the tails of extreme value distributions<sup>42</sup> become heavier in a future climate. This behaviour is consistent at the global domain across all 25 CMIP6 models analysed (Fig. 3) and statistically significant for all SSP scenarios (Supplementary Table S1), as well as for other statistical methods (Supplementary Figs. S10 and S11) and other GCM realisations (Supplementary Figs. S12–S22). Furthermore, these findings are statistically significant for most individual GCMs, particularly for the high emission scenarios (21 out of 25 GCMs for SSP3-7.0 and SSP5-8.5, Supplementary Table S2) and more so for the GCMs with the highest resolutions (Table 1).

Our main result that the magnitude of rarer extremes are expected to increase relatively more is also backed by earlier observation based studies over Australia<sup>47</sup> and over Europe and the USA<sup>22</sup>. As well as based on a single model initial-condition large ensemble study over Western Europe<sup>27</sup>, and on CMIP6 global climate models<sup>15</sup>. The relative magnitude increase is also stronger with higher emission scenarios (see also Table 2), underlying the importance of emission reduction for extreme precipitation hazards.

Figure 4 and Table 2 show where the magnitude of most rare extremes increases relatively more than the common ones, as the difference in relative changes in the 100-year and 1-year return level estimates (see Eq. (4) in “Methods”). Land regions with the largest relative magnitude increase of rare extremes with respect to the common ones are around the subtropics (Sahara and surroundings, Amazon and Central America, and Central and Northern Australia), and oceanic regions include the South Pacific, South Atlantic, South Indian, and to a lesser extent their Northern counterparts. A few regions are exceptions where the common extremes instead are expected to increase relatively more than the rare ones, which are around the Equatorial Pacific Ocean and the poles. For future low-emission SSP scenarios, the models show large spatial discrepancies, contrary to high model agreement for the highest emission scenarios, predominantly over the subtropics. At the high latitudes and tropics, however, the models show more disagreement, which can be explained by more model uncertainty of extreme precipitation over the tropics in general due to the GCM differences<sup>23</sup>.

## Discussion

We showed that in the future rare daily precipitation extremes are expected to increase more than common extremes. The CMIP6 GCMs exhibit high model agreement for this finding in general, particularly for the highest emission scenario (Fig. 4), but some spatial differences exist. The higher the emission scenario, the higher the relative difference found between rare (100-year return level) and common extremes (1-year return level), and with higher statistical significance (Table S1). Particularly we found for low emission scenario SSP1-2.6 and high emission scenario SSP5-8.5 global (land and ocean) daily rainfall extremes will increase by 8.6% and 23.1%, respectively, for 1-year events (Table S3) and by 11.9% and 32.5% for 100-year (Table S4) events by the end of this century. Furthermore, regions are not affected equally, Africa and regions around and just north of the equator particularly will face a disproportionate increase in rare extreme precipitation hazards. This is notably the case for the higher emission scenarios, and much more than the regions most responsible for greenhouse gas emissions that often are expected to have a smaller increase than the global mean (Fig. 2). There are also areas in the subtropical Atlantic and South Pacific oceans that show decreasing precipitation extremes in the future. It should be noted that while the larger patterns of rarer extremes increasing relatively more is quite robust, there are also some regions with

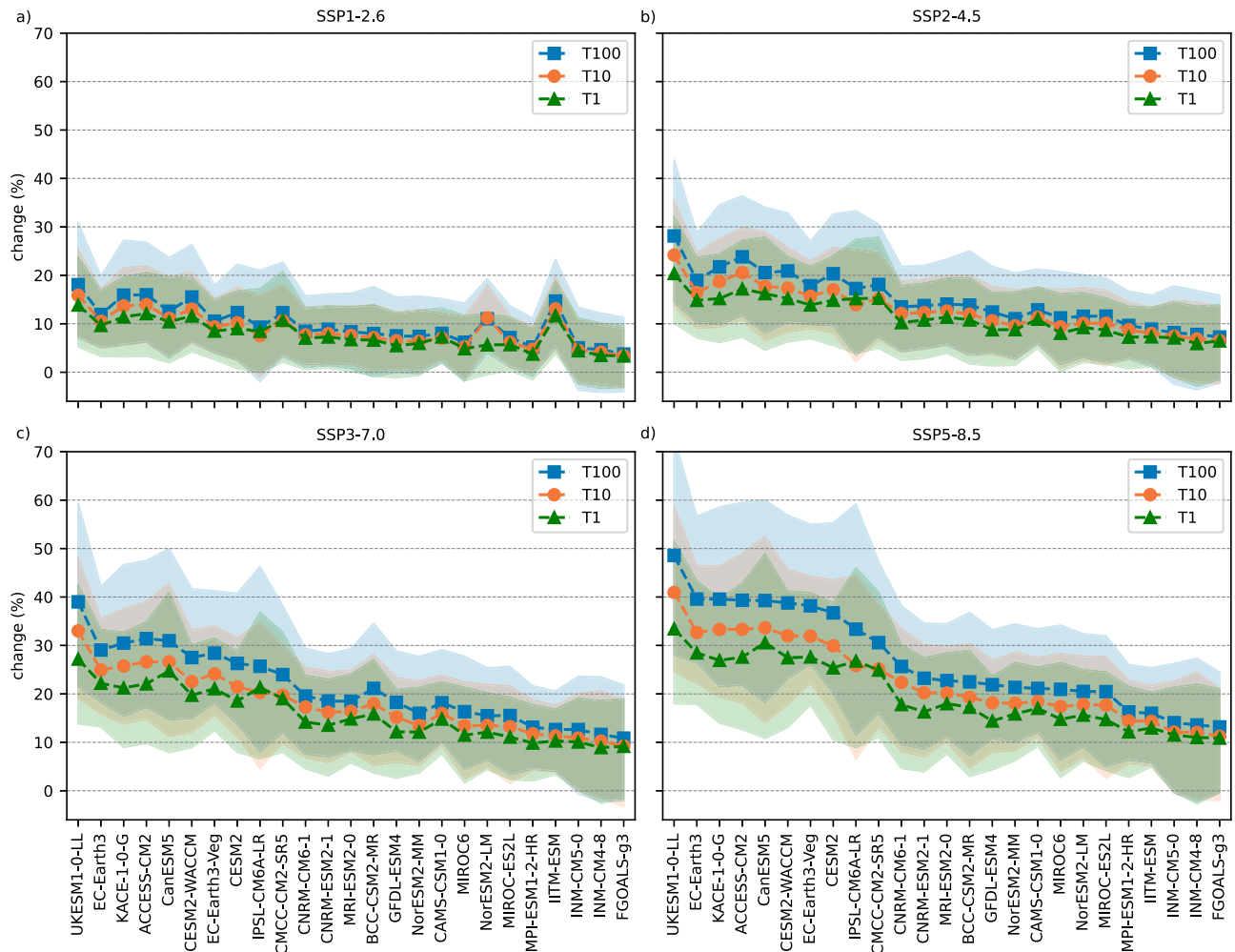


**Fig. 3 Global relative change of precipitation extremes for each individual climate model.** Relative change of daily precipitation extremes simulated using 25 CMIP6 GCMs for the future period (2071–2100) SSP scenario **a** 1–2.6, **b** 2–4.5, **c** 3–7.0 and **d** 5–8.5, with respect to the historical period (1971–2000), Eq. 2. Triangle, circle and square markers respectively represent the global area-weighted median values of the 1, 10 and 100-year return levels. The shaded areas are the area-weighted 25th to 75th percentile intervals. The dashed lines between markers are added for visibility.

model disagreement. For such regions particularly, when compiling future extreme rainfall-intensity-frequency curves a more careful selection and weighting of climate models based on regional observations and advanced bias-correction techniques is advisable.

Here we did not formulate a hypothesis of why we observe this behaviour of rare extremes increasing relative more than common extremes under climate change. Yet, when looking at the changes in the parameters underlying the MEV-Weibull distribution (Eq. (4)), the statistics themselves give some indication about the processes (Supplementary Figs. S23–S25). It should be noted that the behaviour could be caused by either a decrease in the number of wet days  $N$  (combined with an increase in the scale parameter  $C$ )<sup>48</sup> or a decrease in the shape parameter  $W$ , which may, for example, be the result of dynamical feedback processes related to latent heating<sup>49</sup>. It appears that both the rainfall frequency (Supplementary Fig. S23) and dynamical feedback processes (Supplementary Fig. S25) play a role. This may serve as a starting point for future research to further disentangle the processes behind this behaviour. Regardless of the underlying mechanisms, the results of this study have important implications for the design of engineering standards as they are built on the basis of our knowledge of the frequency of precipitation events. If rare extreme precipitation events become more frequent in the

future as suggested here, engineering design standards, such as those used for storm water drainage and other critical water system infrastructure, will need to be updated. Yet, it should be noted that bias correction methods ought to take into account the fact that the rarest quantiles of today's climate are made up of different processes than the rarest quantiles in a future climate. Whereas the challenge of accurately predicting future changes in precipitation has been noted as one of the 'real holes in climate science'<sup>50</sup>, we think that the fact that the model agreement is so high should give confidence in the robustness of our climate models, and our own findings in particular, making that hole just a little bit smaller.

## Methods

**CMIP6 model data.** Daily precipitation simulations from the Coupled Model Intercomparison Project Phase 6 (CMIP6) archive are analysed for the historical and future scenarios. The future late twenty-first century scenarios are Shared Socioeconomic Pathways (SSPs) coupled with the previous Representative Concentration Pathways (RCPs)<sup>33</sup>. We included in our analyses SSP1-2.6, SSP2-4.5, SSP3-7.0 and SSP5-8.5, ranging from the least to the most emissions. The two time periods that are compared are (1) the simulated historical late twentieth century period 1971–2000, and (2) the late twenty-first century period 2071–2100 (or 2070–2099 or 2069–2098, depending on the available climate-model output and ensuring that the latest 30 years leading up to 2100 are used). We use all 25 GCMs that provide complete simulations for the two time periods and all analysed scenarios<sup>51</sup>. For the main analysis we used only one realisation per GCM, but we

**Table 1 Overview of the CMIP6 GCMs and the weights for each GCM included in this study.**

Model	No. of cells (Lat × Lon)	No. of realisations	Institution, country	Weight
ACCESS-CM2	144 × 192	3	CSIRO-ARCCSS, Australia	0.071098
BCC-CSM2-MR	160 × 320	1	BCC, China	0.0375146
CAMS-CSM1-0	160 × 320	1	CAMS, China	0.0205778
CanESM5	64 × 128	50	CCCMA-ECCC, Canada	0.0161621
CESM2	192 × 288	2	NCAR, USA	0.0736632
CESM2-WACCM	192 × 288	1	NCAR, USA	0.0346487
CMCC-CM2-SR5	192 × 288	1	CMCC, Italy	0.0414861
CNRM-CM6-1	128 × 256	1	CNRM-CERFACS, France	0.0350501
CNRM-ESM2-1	128 × 256	1	CNRM-CERFACS, France	0.0547842
EC-Earth3	256 × 512	7	EC-Earth consortium	0.0016417
EC-Earth3-Veg	256 × 512	4	EC-Earth consortium	0.0834485
FGOALS-g3	80 × 180	3	LASG-IAP-CAS, China	0.0091949
GFDL-ESM4	180 × 288	1	GFDL-NOAA, USA	0.1476730
IITM-ESM	94 × 192	1	CCCR-IITM, India	0.0372205
INM-CM4-8	120 × 180	1	INM-RAS, Russia	0.0141569
INM-CM5-0	120 × 180	1	INM-RAS, Russia	0.0323639
IPSL-CM6A-LR	143 × 144	6	IPSL, France	0.0362602
KACE-1-0-G	144 × 192	3	NIMS/KMA, Republic of Korea	0.0497750
MIROC6	128 × 256	3	CCSR-UT-JAMSTEC-NIES, Japan	0.0668575
MIROC-ES2L	64 × 128	1	CCSR-UT-JAMSTEC-NIES, Japan	0.0093852
MPI-ESM1-2-HR	192 × 384	1	MPI, Germany	0.0504672
MRI-ESM2-0	160 × 320	2	MRI, Japan	0.0302788
NorESM2-LM	96 × 144	1	NCC, Norway	0.0199261
NorESM2-MM	192 × 288	1	NCC, Norway	0.0201326
UKESM1-0-LL	144 × 192	5	MO-NERC, UK	0.0062219

also analysed all the different realisations with complete simulations for all five scenarios (one historical and four SSP scenarios, see Supplementary Figs. S12–S22). We arbitrarily selected the first available realisation of each GCM, however, the similarity between different realisations (Supplementary Figs. S12–S22) led us to believe that this did not affect our main findings. An overview of the models is displayed in Table 1. As there are large differences in the resolution of the different GCMs, the analyses are performed on each model’s native grid. The results are then remapped to a 0.25° × 0.25° grid using the nearest neighbour interpolation method for the ensemble means. The results remain mostly unaffected by the remapping, as the 0.25° × 0.25° grid is a higher resolution than the native grid of each of the models. Specifically, the remapped grid-cells are 4 to 63 times smaller depending on the model resolution, and as we used nearest neighbour interpolation no spatial averaging is taking place. Moreover, as the main results of this study are relative values instead of absolute values, the different resolutions of the models do not influence these results.

**Model weighting.** To account for GCM performance as well as model interdependencies in the used multi-model ensemble, we apply the Climate model Weighting by Independence and Performance (ClimWIP) method<sup>35–37,52</sup>. ClimWIP assigns a weight  $w_i$  to each model to account for the models’ performance in simulating historical climate ( $D_i$ ) and independence from the other models ( $j = 1...M$ ) in the ensemble ( $S_{ij}$ ):

$$w_i = \frac{e^{-\left(\frac{D_i}{\sigma_D}\right)^2}}{1 + \sum_{j \neq i}^M e^{-\left(\frac{S_{ij}}{\sigma_S}\right)^2}}, \quad (1)$$

with the shape parameters  $\sigma_D$  and  $\sigma_S$  determining the strength of the performance and independence weighting, respectively (see ref. <sup>35</sup> for more details). We use an implementation of ClimWIP within the Earth System Model Evaluation Tool (ESMValTool)<sup>53</sup> version 2.3<sup>54</sup>.

The independence weighting is based on model–model distances in 1979–2014 climatologies of temperature and sea level pressure in the same setup as used by Brunner et al.<sup>35</sup> but updated for the 25 GCMs used in this study. These metrics have been shown to cluster models by known development families and account for dependencies<sup>35,52</sup>.

For model performance, we adapted the metrics used in ref. <sup>35</sup> to the target of global precipitation change. In contrast to other important climate variables, most prominently future warming<sup>35,55–57</sup>, emergent constraints<sup>58</sup> for global precipitation changes have only recently been suggested<sup>59,60</sup>. Here, our main aim was to reduce the influence of models which simulate variables considered important for the representation of precipitation very different from observations rather than applying a constraint that necessarily reduces model spread. Performance weights were, therefore, based on five metrics: (1) the temperature trend, which has been found to be an important constraint for temperature and

precipitation changes alike<sup>55,59</sup>, (2) the temperature climatology, (3) the variability of temperature, (4) the precipitation climatology and (5) the variability of precipitation, all in the period 1979–2014. Models which perform poorly in one or more of these metrics received less weight in the calculation of multi-model statistics as we trust their projections of future precipitation less. The strength of the weighting was established using a leave-one-out model-as-truth test<sup>35,37,61</sup> on the target of global mean precipitation change. The resulting weights for each model are included in Table 1 and have a range comparable to recent studies, such as Brunner et al.<sup>35</sup> (their Table S2 in the supplement). The weights of the models were used to create the multi-model weighted ensemble means for Figs. 1, 2, 4, and Supplementary Figs. S3, S7–S9, and S23–S25.

**Changes in precipitation estimates.** To study if the relative change in common extremes is different from the relative change in rare extremes, we use the following two equations:

$$C_{rel,t,x} = \frac{T_{t,SSPx} - T_{t,historical}}{T_{t,historical}} \quad (2)$$

$$D_{100-1,x} = C_{rel,100,x} - C_{rel,1,x} = \frac{T_{100,SSPx} - T_{100,historical}}{T_{100,historical}} - \frac{T_{1,SSPx} - T_{1,historical}}{T_{1,historical}} \quad (3)$$

With Eq. (2) we estimate ( $C_{rel,t,x}$ ), which is the relative change between historical and future precipitation for each of the return levels ( $T_t$ ) and for any SSP scenario (SSPx). We use Eq. (2) as input for Eq. (3), where  $D_{100-1,x}$  stands for the difference in change of rare and common extremes,  $T_{100}$  stands for the 100-year return level and  $T_1$  for the 1-year return level. For the all-day percentile method the same formula applies, but  $T_{100}$  and  $T_1$  were substituted by  $T_{30}$  and  $T_{0.3}$ .

**Extreme precipitation estimates.** In this study, we estimated the common and rare extreme precipitation at each model grid-cell using three different methods: (1) the Metastatistical Extreme Value (MEV) distribution, (2) the Generalised Extreme Value (GEV) distribution, and (3) quantiles directly obtained from the precipitation simulations of all models. By using different methods for the calculation of precipitation extremes, we show the robustness of our results and allow for comparison with other studies.

The rare precipitation extremes (with return levels of 10 and 100 years) we present in this paper are calculated using the first method: the MEV distribution<sup>41</sup>. As opposed to traditional extreme value distributions, MEV uses all available data, and is, therefore, able to estimate return periods higher than the period of record with reduced uncertainty if the tail of the true distribution matches<sup>40,62–64</sup>, and shows more consistent geographical patterns than traditional methods as GEV<sup>42,43,62</sup>. Following the approach of Zorzetto et al.<sup>40</sup>, for each individual year the Weibull distribution is fitted to all days with a precipitation depth exceeding 1

**Table 2 Regional difference in weighted mean change for the 100- (Supplementary Table S4) and 1-year return levels (Supplementary Table S3) between the historical (1971–2000) and four future SSP scenarios (2071–2100).**

Abbreviation	Region	SSP1-2.6	SSP2-4.5	SSP3-7.0	SSP5-8.5
SAH	Sahara	10.69	18.81	24.93	34.45
WAF	Western-Africa	3.62	8.29	19.30	25.71
CAU	C.Australia	12.27	11.94	18.54	23.56
SCA	S.Central-America	4.28	7.17	12.92	22.29
CAF	Central-Africa	3.51	6.69	15.35	21.44
NSA	N.South-America	4.60	9.75	15.78	21.09
NAU	N.Australia	8.69	12.20	15.43	19.65
SPO	S.Pacific-Ocean	7.72	12.85	16.14	19.52
NCA	N.Central-America	7.25	10.62	16.15	19.31
MDG	Madagascar	6.39	8.21	13.72	19.06
NES	N.E.South-America	4.35	7.03	13.37	19.00
SAO	S.Atlantic-Ocean	8.04	11.00	13.55	18.58
SAM	South-American-Monsoon	4.98	9.03	14.27	18.56
WSAF	W.Southern-Africa	8.13	11.05	13.78	18.55
MED	Mediterranean	6.27	9.34	15.13	17.96
SAS	S.Asia	3.07	5.10	12.04	17.84
ESAF	E.Southern-Africa	7.23	9.16	14.23	17.70
SAU	S.Australia	4.89	8.94	13.85	17.32
SWS	S.W.South-America	6.64	10.07	12.51	16.51
SIO	S.Indic-Ocean	5.44	8.67	12.53	15.33
EAU	E.Australia	3.99	6.63	11.78	13.90
NWS	N.W.South-America	3.45	8.12	9.73	13.43
NAO	N.Atlantic-Ocean	5.33	7.74	10.52	12.69
NZ	New-Zealand	3.70	5.82	10.11	11.73
SSA	S.South-America	2.51	6.10	8.05	11.39
-	Global (land)	3.06	4.96	8.25	10.65
SES	S.E.South-America	3.21	5.37	7.87	10.48
SEA	S.E.Asia	1.95	3.47	7.94	10.40
WCA	W.C.Asia	2.96	5.44	8.29	9.87
NEAF	N.Eastern-Africa	4.23	7.98	10.86	9.81
CAR	Caribbean	2.24	4.84	8.64	9.74
-	Global (all)	3.31	5.18	7.54	9.61
EAS	E.Asia	1.14	3.10	6.36	8.62
NPO	N.Pacific-Ocean	3.10	4.63	7.01	8.56
BOB	Bay-of-Bengal	2.09	1.46	4.45	8.12
WCE	West&Central-Europe	2.55	3.86	5.78	8.06
SEAF	S.Eastern-Africa	1.97	2.60	6.34	7.50
CNA	C.North-America	1.70	3.26	4.69	6.82
ARP	Arabian-Peninsula	6.40	9.00	11.48	6.76
SOO	Southern-Ocean	1.55	2.74	4.64	6.26
ENA	E.North-America	1.59	3.04	4.85	6.22
TIB	Tibetan-Plateau	0.95	1.17	3.64	5.99
WNA	W.North-America	2.28	2.81	4.57	5.57
EIO	Equatorial.Indic-Ocean	1.24	1.51	2.71	5.47
EEU	E.Europe	1.74	2.35	3.66	5.28
NEU	N.Europe	1.28	2.20	2.59	4.05
EAO	Equatorial.Atlantic-Ocean	0.21	0.64	3.70	3.29
RFE	Russian-Far-East	0.66	1.01	2.45	3.14
EAN	E.Antarctica	1.08	2.43	2.27	2.63
ECA	E.C.Asia	0.72	0.12	0.14	2.24
WSB	W.Siberia	0.11	-0.16	0.50	1.67
GIC	Greenland/Iceland	0.71	0.39	1.19	1.32
WAN	W.Antarctica	0.33	0.62	0.96	1.32
NWN	N.W.North-America	0.10	-0.08	0.64	1.04

**Table 2 (continued)**

Abbreviation	Region	SSP1-2.6	SSP2-4.5	SSP3-7.0	SSP5-8.5
ESB	E.Siberia	0.05	0.04	0.43	0.97
NEN	N.E.North-America	0.26	0.56	0.91	0.79
ARS	Arabian-Sea	2.12	-1.14	-3.46	-5.45
RAR	Russian-Arctic	-2.08	-3.45	-4.75	-6.04
ARO	Arctic-Ocean	-2.96	-4.17	-5.70	-6.74
EPO	Equatorial.Pacific-Ocean	-2.19	-4.33	-8.78	-11.11

The regions in the table are the IPCC WGI reference regions (version 4)<sup>69</sup>, as well as global land cells and all global cells (italic). Values are ordered in descending order for SSP5-8.5. A positive change indicates that the 100-year return levels will increase relatively more than the 1-year return level.

mm. Years are grouped together if the number of events per year is lower than twenty, to allow for more accurate parameter estimation<sup>65</sup>. The Weibull parameters are fitted using probability-weighted moments<sup>66</sup>. The cumulative distribution function of MEV-Weibull is as follows:

$$\zeta_m(x) = \frac{1}{M} \sum_{j=1}^M \left\{ 1 - \exp \left[ - \left( \frac{x}{C_j} \right)^{w_j} \right] \right\}^{n_j} \tag{4}$$

where  $j$  is the year ( $j = 1, 2, \dots, M$ ),  $C_j > 0$  is the Weibull scale parameter,  $w_j > 0$  is the Weibull shape parameter, and  $n_j$  is the number of wet events in hydrological year  $j$ <sup>41</sup>.

The second method to calculate the rare extremes is using the traditional GEV distribution. Annual maxima are used to estimate the GEV parameters with the L-moments approach<sup>67</sup>. The cumulative distribution function of GEV is:

$$G(z) = \begin{cases} \exp \left\{ - \left[ 1 + \xi \left( \frac{z-\mu}{\sigma} \right) \right]^{-\xi} \right\}, \xi \neq 0 \\ \exp \left\{ - \exp \left[ - \left( \frac{z-\mu}{\sigma} \right) \right] \right\}, \xi = 0 \end{cases} \tag{5}$$

with location parameter  $\mu \in (-\infty, \infty)$ , scale parameter  $\sigma > 0$ , and shape parameter  $\xi \in (-\infty, \infty)$ . The results for GEV are included in Supplementary Fig. S10.

The third method is to obtain the precipitation extremes directly from the precipitation estimation of each model, using all-day percentiles. The common extremes we present in this paper, the ones with a return level of 1 year (99.7262th percentile), are directly estimated from the precipitation time series for each grid-cell. This is because extreme value distributions are designed for return levels greater than the length of the time series. We also estimated the precipitation depths for all-day percentiles corresponding to the 0.3-year (approximately once every 109 days), 3-year, and 30-year (highest value in the 30-year time-series) return levels: the 99.0874th, 99.9087th, and 99.9909th percentile respectively. For the 30-year return level it is particularly uncertain whether the maximum observed precipitation event actually represents an event with a 30-year return period, which is why we did not use this as a primary method. Yet, averaged over large regions or globally this approach can still be considered valid. The results for this method are included in Supplementary Fig. S11.

**Statistical analysis.** To determine whether the results found that rarest extremes will increase more than the common ones ( $D_{100-1,x} > 0$ , Eq. (3)) are statistically significant, we followed Livezey and Chen<sup>68</sup>. To account for spatial correlation, we first calculated the number of spherical harmonics that explain 95% of the observed variation in change in T1 ( $C_{rel,1,x}$ , Eq. (2)) and change in T100 ( $C_{rel,100,x}$ , Eq. (2)) for each of the 25 GCMs and SSP scenarios. The degrees of freedom in these data were set to be equal to this number of harmonics. Note that the lower the percentage used, the more conservative the test will be, with 95% being conservative. We then drew a number, equal to the degrees of freedom, of random samples from the change in T1 and T100 estimates for each GCM and SSP scenario, and calculated the median of these samples. The drawing excluded masked pixels (weighted mean of less than 3 events per year, see Section Mask dry areas) and was weighted according to the area of the pixels. This analysis was done as a monte carlo (mc) simulation and repeated 10,000 times to determine the Cumulative Distribution Function of the median of samples of size degrees of freedom of randomly chosen pixels. Finally, the values that exceeded 5%, 2%, and 1% of the medians of the samples, were taken as the 95%, 98%, and 99% confidence levels with which the null-hypothesis that there was no increase could be rejected.

We also applied the Spearman's rank correlation to analyse whether the median change in the monte carlo 100-year return level ( $mc-C_{rel,100,x}$ , Eq. (2)) is significantly larger than the median change in the monte carlo 1-year return level ( $mc-C_{rel,1,x}$ ). We assumed that each GCM is an independent experiment resulting in an estimate for  $mc-C_{rel,100,x}$  and  $mc-C_{rel,1,x}$ . The null-hypothesis is that there is no statistical relationship between the change and being a member of either the  $mc-C_{rel,100,x}$  or the  $mc-C_{rel,1,x}$  family (i.e.,  $mc-C_{rel,100,x} = mc-C_{rel,1,x}$ ). We tested

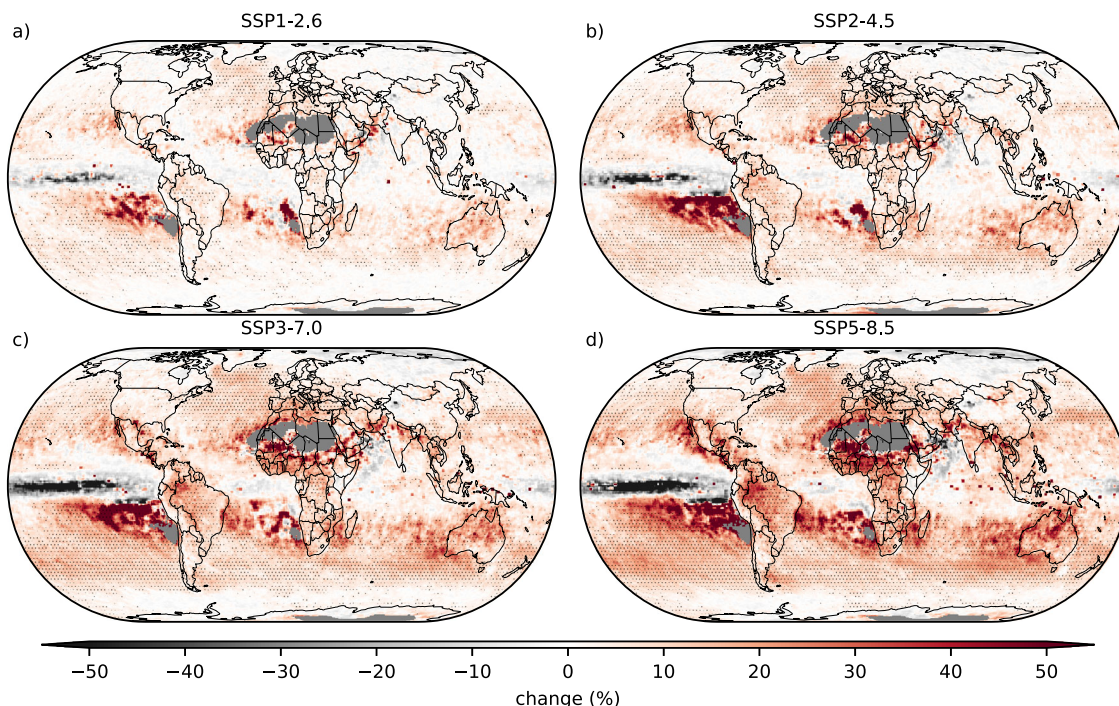


**Fig. 4** Difference in future changes between rare and common extremes. Difference in weighted mean change for the 100- and 1-year return levels between the historical and future SSP scenarios **a** 1-2.6, **b** 2-4.5, **c** 3-7.0 and **d** 5-8.5. Panel **d** is the difference of Fig. 2c and a. A positive change indicates that the 100-year return levels will increase relatively more than the 1-year return level (Eq. (3)). The hatching represents areas where more than 75% of the models agree on the sign of change. Dry areas (weighted mean of less than 3 events per year) are masked in grey.

whether the changes in 100-year return levels are significantly larger than the changes in 1-year return levels at 99%, 99.9%, and 99.99% significance levels.

**Mask dry areas.** Estimating the difference between common and rare extremes for highly arid places, such as the Sahara, makes little sense as precipitation occurs so seldom. Therefore, we created a mask to remove very dry areas from our study, based on the mean number of dry events per year combined with the performance-based weights for each model. We calculated the mean number of events per year for each of the 25 models, each individual pixel, and for the one historical and four future scenarios. We used this information to create a mask per model and scenario, with a 1 if the number of events is equal to or exceeds three events per year, and a 0 if there are less than three events per year. These individual masks are then remapped to a  $0.25^\circ \times 0.25^\circ$  grid using the nearest neighbour interpolation method. The masks for the individual models and scenarios, consisting of 0 and 1 values, are multiplied by the performance-based weights for each model. After which, the sum of the 25 weighted masks for each pixel and each individual scenario is taken. If the sum of the 25 weighted masks is equal to or greater than 0.75 at the pixel level, that pixel will get the value of 1. If the sum of the weighted masks is smaller than 0.75, that pixel will get the value of 0. This results in five masks with values of 0 and 1: one for the historical scenario and four for the SSP scenarios. The final mask is created by multiplying all five masks, to ensure that there are on average 3 events per year for all individual scenarios. The areas where there are not enough events per year are marked as grey on the maps, and these pixels are not considered for any analyses.

**Regional analysis.** We conducted the regional analysis based on the Intergovernmental Panel on Climate Change Working Group I (IPCC WGI) reference regions, version 4<sup>69</sup>. Supplementary Fig. S26 shows an overview of the geographical locations of these reference regions, whereas the region name corresponding to the abbreviations are included in Table 2. The IPCC WGI reference regions were chosen in order to allow for consistency with other scientific research. These IPCC WGI regions were used to calculate the weighted multi-model ensemble regional means, for Table 1, and Supplementary Tables S3 and S4. Furthermore, weights were applied to reflect the cell sizes, so that cells with larger land masses (around the equator) get higher weights than the cells with small land masses (higher latitudes around the poles).

#### Data availability

The data for producing the graphs and charts in this manuscript are publicly available in the 4TU repository<sup>70</sup>: <https://doi.org/10.4121/20531376>. The CMIP6 data that support

the findings of this study are openly available from the Earth System Grid Federation (ESGF) archive<sup>51</sup>: <https://esgf-data.dkrz.de/search/cmip6-dkrz/>. See CMIP6 Data References at page 26 in the Supplementary Information for the references of each individual model and scenario that were analysed in this study.

#### Code availability

The codes to create the graphs and charts in this manuscript are publicly available in the 4TU repository<sup>70</sup>: <https://doi.org/10.4121/20531376>. We used the mevpy Python package (<https://github.com/EnricoZorzetto/mevpy>) for the extreme value analysis, and regmask Python package for the regional analysis. For the spherical harmonics calculations, we used pyshtools (<https://shtools.github.io/SHTOOLS/real-spherical-harmonics.html>). To analyse the data and create the graphs and charts, we also used the following python packages: cartopy, matplotlib, netCDF4, numpy, pandas, string, and xarray. For the model weighting we used an implementation of ClimWIP within the Earth System Model Evaluation Tool (ESMValTool)<sup>53</sup> version 2.3<sup>54</sup> ([https://docs.esmvaltool.org/en/latest/recipes/recipe\\_climwip.html](https://docs.esmvaltool.org/en/latest/recipes/recipe_climwip.html)). In order to remap the data to a common grid, we used the Climate Data Operator (CDO) “remapnn” by the Max-Planck Institute.

Received: 17 January 2022; Accepted: 20 September 2022;

Published online: 10 October 2022

#### References

- Allen, M. R. & Ingram, W. J. Constraints on future changes in climate and the hydrologic cycle. *Nature* **419**, 224–232 (2002).
- Papalexiou, S. M. & Montanari, A. Global and regional increase of precipitation extremes under global warming. *Water Resour. Res.* **55**, 4901–4914 (2019).
- Alexander, L. V. Global observed long-term changes in temperature and precipitation extremes: a review of progress and limitations in IPCC assessments and beyond. *Weather Clim. Extremes* **11**, 4–16 (2016).
- Donat, M. G., Alexander, L. V., Herold, N. & Dittus, A. J. Temperature and precipitation extremes in century-long gridded observations, reanalyses, and atmospheric model simulations. *J. Geophys. Res. Atmosph.* **121**, 174–189 (2016).
- Asadieh, B. & Krakauer, N. Y. Global trends in extreme precipitation: climate models versus observations. *Hydrol. Earth Syst. Sci.* **19**, 877–891 (2015).

6. Westra, S., Alexander, L. V. & Zwiers, F. W. Global increasing trends in annual maximum daily precipitation. *J. Clim.* **26**, 3904–3918 (2013).
7. Moustakis, Y., Papalexiou, S. M., Onof, C. J. & Paschalis, A. Seasonality, intensity, and duration of rainfall extremes change in a warmer climate. *Earth's Future* **9**, 1–15 (2021).
8. Myhre, G. et al. Frequency of extreme precipitation increases extensively with event rareness under global warming. *Nat. Sci. Rep.* **9**, 1–10 (2019).
9. Donat, M. G., Lowry, A. L., Alexander, L. V., Gorman, P. A. O. & Maher, N. More extreme precipitation in the world's dry and wet regions. *Nat. Clim. Change* **6**, 508–513 (2016).
10. Kharin, V. V., Zwiers, F. W., Zhang, X. & Wehner, M. Changes in temperature and precipitation extremes in the CMIP5 ensemble. *Clim. Change* **119**, 345–357 (2013).
11. Sillmann, J., Kharin, V. V., Zwiers, F. W., Zhang, X. & Bronaugh, D. Climate extremes indices in the CMIP5 multimodel ensemble: Part 2. Future climate projections. *J. Geophys. Res. Atmosph.* **118**, 2473–2493 (2013).
12. Westra, S. et al. Future changes to the intensity and frequency of short-duration extreme rainfall. *Rev. Geophys.* **52**, 522–555 (2014).
13. Loriaux, J. M., Lenderink, G., De Roode, S. R. & Siebesma, A. P. Understanding convective extreme precipitation scaling using observations and an entraining plume model. *J. Atmosph. Sci.* **70**, 3641–3655 (2013).
14. Eyring, V. et al. Overview of the Coupled Model Intercomparison Project Phase 6 (CMIP6) experimental design and organization. *Geosci. Model Dev.* **9**, 1937–1958 (2016).
15. Li, C. et al. Changes in annual extremes of daily temperature and precipitation in CMIP6 models. *J. Clim.* **34**, 3441–3460 (2021).
16. Mehrotra, R. & Sharma, A. A robust alternative for correcting systematic biases in multi-variable climate model simulations. *Environ. Model. Softw.* **139**, 105019 (2021).
17. Photiadou, C., van den Hurk, B., van Delden, A. & Weerts, A. Incorporating circulation statistics in bias correction of GCM ensembles: hydrological application for the Rhine basin. *Clim. Dyn.* **46**, 187–203 (2016).
18. Johnson, F. & Sharma, A. A nesting model for bias correction of variability at multiple time scales in general circulation model precipitation simulations. *Water Resour. Res.* **48**, 1–16 (2012).
19. Borodina, A., Fischer, E. M. & Knutti, R. Models are likely to underestimate increase in heavy rainfall in the extratropical regions with high rainfall intensity. *Geophys. Res. Lett.* **44**, 7401–7409 (2017).
20. Scoccimarro, E. & Gualdi, S. Heavy daily precipitation events in the CMIP6 worst-case scenario: Projected twenty-first-century changes. *J. Clim.* **33**, 7631–7642 (2020).
21. Pendergrass, A. G. & Knutti, R. The uneven nature of daily precipitation and its change. *Geophys. Res. Lett.* **45**, 980–988 (2018).
22. Fischer, E. M. & Knutti, R. Observed heavy precipitation increase confirms theory and early models. *Nat. Clim. Change* **6**, 986–991 (2016).
23. Bador, M., Donat, M. G., Geoffroy, O. & Alexander, L. V. Assessing the robustness of future extreme precipitation intensification in the CMIP5 ensemble. *J. Clim.* **31**, 6505–6525 (2018).
24. Alexander, L. V. & Arblaster, J. M. Historical and projected trends in temperature and precipitation extremes in Australia in observations and CMIP5. *Weather Clim. Extremes* **15**, 34–56 (2017).
25. Dong, S. et al. Attribution of extreme precipitation with updated observations and CMIP6 simulations. *J. Clim.* **34**, 871–881 (2021).
26. Maher, N., Milinski, S. & Ludwig, R. Large ensemble climate model simulations: introduction, overview, and future prospects for utilising multiple types of large ensemble. *Earth Syst. Dyn.* **12**, 401–418 (2021).
27. Aalbers, E. E., Lenderink, G., van Meijgaard, E. & van den Hurk, B. J. J. M. Local-scale changes in mean and heavy precipitation in Western Europe, climate change or internal variability? *Clim. Dyn.* **50**, 4745–4766 (2018).
28. Olsson, J., Södling, J., Berg, P., Wern, L. & Eronn, A. Short-duration rainfall extremes in Sweden: A regional analysis. *Hydrol. Res.* **50**, 945–960 (2019).
29. Overeem, A., Buishand, A. & Holleman, I. Rainfall depth-duration-frequency curves and their uncertainties. *J. Hydrol.* **348**, 124–134 (2008).
30. Hodnebrog, Ø. et al. Intensification of summer precipitation with shorter time-scales in Europe. *Environ. Res. Lett.* **14**, 124050 (2019).
31. Chan, S. C., Kahana, R., Kendon, E. J. & Fowler, H. J. Projected changes in extreme precipitation over Scotland and Northern England using a high-resolution regional climate model. *Clim. Dyn.* **51**, 3559–3577 (2018).
32. DeGaetano, A. T. & Castellano, C. M. Future projections of extreme precipitation intensity-duration-frequency curves for climate adaptation planning in New York State. *Clim. Serv.* **5**, 23–35 (2017).
33. O'Neill, B. C. et al. The Scenario Model Intercomparison Project (ScenarioMIP) for CMIP6. *Geosci. Model Dev.* **9**, 3461–3482 (2016).
34. Lee, J. Y. et al. Future global climate: scenario-based projections and near-term information. In *Climate Change 2021: The Physical Science Basis. Contribution of Working Group I to the Sixth Assessment Report of the Intergovernmental Panel on Climate Change* (eds Masson-Delmotte, V. et al.) (Cambridge University Press, 2021).
35. Brunner, L. et al. Reduced global warming from CMIP6 projections when weighting models by performance and independence. *Earth Syst. Dyn.* **11**, 995–1012 (2020).
36. Lorenz, R. et al. Prospects and caveats of weighting climate models for summer maximum temperature projections over North America. *J. Geophys. Res. Atmosph.* **123**, 4509–4526 (2018).
37. Knutti, R. et al. A climate model projection weighting scheme accounting for performance and interdependence: Model Projection Weighting Scheme. *Geophys. Res. Lett.* **44**, 1909–1918 (2017).
38. Sanderson, B. M., Knutti, R. & Caldwell, P. Addressing interdependency in a multimodel ensemble by interpolation of model properties. *J. Clim.* **28**, 5150–5170 (2015).
39. Sanderson, B. M., Knutti, R. & Caldwell, P. A representative democracy to reduce interdependency in a multimodel ensemble. *J. Clim.* **28**, 5171–5194 (2015).
40. Zorzetto, E., Botter, G. & Marani, M. On the emergence of rainfall extremes from ordinary events. *Geophys. Res. Lett.* **43**, 8076–8082 (2016).
41. Marani, M. & Ignaccolo, M. A metastatistical approach to rainfall extremes. *Adv. Water Resour.* **79**, 121–126 (2015).
42. Gründemann, G. J. et al. Extreme precipitation return levels for multiple durations on a global scale. *Earth Space Sci. Open Arch.* **24**, 1–24 (2020).
43. Zorzetto, E. & Marani, M. Extreme value metastatistical analysis of remotely sensed rainfall in ungauged areas: Spatial downscaling and error modelling. *Adv. Water Resour.* **135**, 103483 (2020).
44. O'Gorman, P. A. Precipitation extremes under climate change. *Curr. Clim. Change Rep.* **1**, 49–59 (2015).
45. Pfahl, S., Gorman, P. A. O. & Fischer, E. M. Understanding the regional pattern of projected future changes in extreme precipitation. *Nat. Clim. Change* **7**, 423–428 (2017).
46. Ali, H., Peleg, N. & Fowler, H. J. Global scaling of rainfall with dewpoint temperature reveals considerable ocean-land difference. *Geophys. Res. Lett.* **48**, e2021GL093798 (2021).
47. Guerreiro, S. B. et al. Detection of continental-scale intensification of hourly rainfall extremes. *Nat. Clim. Change* **8**, 803–807 (2018).
48. Schär, C. et al. Percentile indices for assessing changes in heavy precipitation events. *Clim. Change* **137**, 201–216 (2016).
49. Nie, J., Sobel, A. H., Shaevitz, D. A. & Wang, S. Dynamic amplification of extreme precipitation sensitivity. *Proc. Natl Acad. Sci. USA* **115**, 9467–9472 (2018).
50. Schiermeier, Q. The real holes in climate science. *Nature* **463**, 284–287 (2010).
51. ESGF. World Climate Research Programme - CMIP6 data. <https://esgf-node.llnl.gov/search/cmip6/>, last accessed on 01/12/2020.
52. Merrifield, A. L., Brunner, L., Lorenz, R., Medhaug, I. & Knutti, R. An investigation of weighting schemes suitable for incorporating large ensembles into multi-model ensembles. *Earth Syst. Dynamics* **11**, 807–834 (2020).
53. Eyring, V. et al. Earth System Model Evaluation Tool (ESMValTool) v2.0 - an extended set of large-scale diagnostics for quasi-operational and comprehensive evaluation of Earth system models in CMIP. *Geosci. Model Dev.* **13**, 3383–3438 (2020).
54. Andela, B. et al. ESMValTool. <https://github.com/ESMValGroup/ESMValTool/> (2021).
55. Tokarska, K. B. et al. Past warming trend constrains future warming in CMIP6 models. *Sci. Adv.* **6**, eaz9549 (2020).
56. Nijse, F. J. M. M., Cox, P. M. & Williamson, M. S. Emergent constraints on transient climate response (TCR) and equilibrium climate sensitivity (ECS) from historical warming in CMIP5 and CMIP6 models. *Earth Syst. Dyn.* **11**, 737–750 (2020).
57. Zelinka, M. D. et al. Causes of higher climate sensitivity in CMIP6 models. *Geophys. Res. Lett.* **47**, e2019GL085782 (2020).
58. Hall, A., Cox, P., Huntingford, C. & Klein, S. Progressing emergent constraints on future climate change. *Nat. Clim. Change* **9**, 269–278 (2019).
59. Shiogama, H., Watanabe, M., Kim, H. & Hirota, N. Emergent constraints on future precipitation changes. *Nature* **602**, 612–616 (2022).
60. Thackeray, C. W., Hall, A., Norris, J. & Chen, D. Constraining the increased frequency of global precipitation extremes under warming. *Nat. Clim. Change* **12**, 441–448 (2022).
61. Brunner, L., Lorenz, R., Zumwald, M. & Knutti, R. Quantifying uncertainty in European climate projections using combined performance-independence weighting. *Environ. Res. Lett.* **14**, 124010 (2019).
62. Marra, F., Nikolopoulos, E. I., Anagnostou, E. N., Bárdossy, A. & Morin, E. Precipitation frequency analysis from remotely sensed datasets: a focused review. *J. Hydrol.* **574**, 699–705 (2019).
63. Schellander, H., Lieb, A. & Hell, T. Error structure of metastatistical and generalized extreme value distributions for modeling extreme rainfall in Austria. *Earth Space Sci.* **6**, 1616–1632 (2019).



64. Marra, F., Nikolopoulos, E. I., Anagnostou, E. N. & Morin, E. Metastatistical Extreme Value analysis of hourly rainfall from short records: estimation of high quantiles and impact of measurement errors. *Adv. Water Resour.* **117**, 27–39 (2018).
65. Miniussi, A. & Marani, M. Estimation of daily rainfall extremes through the metastatistical extreme value distribution: Uncertainty minimization and implications for trend detection. *Water Resour. Res.* **56**, e2019WR026535 (2020).
66. Greenwood, J. A., Landwehr, J., Matalas, N. & Wallis, J. Probability weighted moments: definition and relation to parameters of several distributions expressible in inverse form. *Water Resour. Res.* **15**, 1049–1054 (1979).
67. Hosking, J. R. M. L-Moments: Analysis and estimation of distributions using linear combinations of order statistics. *J. R. Statist. Soc. Ser. B (Methodol.)* **52**, 105–124 (1990).
68. Livezey, R. E. & Chen, W. Y. Statistical field significance and its determination by Monte Carlo techniques. *Mon. Weather Rev.* **11**, 46–59 (1983).
69. Iturbide, M. et al. An update of IPCC climate reference regions for subcontinental analysis of climate model data: Definition and aggregated datasets. *Earth Syst. Sci. Data* **12**, 2959–2970 (2020).
70. Gründemann, G. J., van de Giesen, N., Brunner, L. & van der Ent, R. Scripts and data for “rarest rainfall events will see the greatest relative increase in magnitude under future climate change”. *4TU Research Data* <https://doi.org/10.4121/20531376> (2022).

## Acknowledgements

We acknowledge the World Climate Research Programme, which is responsible for CMIP6. We thank the climate modelling groups for making available their model output, the Earth System Grid Federation (ESGF) for archiving the data and providing access, and the multiple funding agencies who support CMIP6 and ESGF. We acknowledge each individual model and scenario that we analysed in this study, a list of which is included in the CMIP6 Data References section of the Supplementary Information (pages 26–33). This work was carried out on the Dutch National e-Infrastructure (DNI) with support from the SURF cooperative. N.G. acknowledges support of the European Commission’s Horizon 2020 Programme under grant agreement number 776691 (TWIGA). L.B. was supported by the EUCP project, funded by the European Commission through the Horizon 2020 Programme for Research and Innovation (grant no. 776613). R.E. acknowledges funding from the Netherlands Organization for Scientific Research (NWO), project number 016.Veni.181.015. G.G. thanks Martyn Clark for the support during her stay at the Coldwater Laboratory. Furthermore, we thank Ruth Lorenz for the fruitful discussions and two reviewers for their insightful comments that helped to improve this manuscript.

## Author contributions

Conceptualisation: G.G., R.E. Methodology: G.G., N.G., L.B., R.E. Software: G.G., N.G., L.B., R.E. Validation: G.G., N.G., L.B., R.E. Formal analysis: G.G., N.G., L.B., R.E. Data curation: G.G. Writing - original draft: G.G., R.E. Writing - review & editing: G.G., N.G., L.B., R.E. Visualisation: G.G. Supervision: R.E.. Project Administration: G.G., R.E. Funding Acquisition: R.E., N.G., L.B.

## Competing interests

The authors declare no competing interests.

## Additional information

**Supplementary information** The online version contains supplementary material available at <https://doi.org/10.1038/s43247-022-00558-8>.

**Correspondence** and requests for materials should be addressed to Gaby Joanne Gründemann.

**Peer review information** *Communications Earth & Environment* thanks Simon Papalexiou and the other, anonymous, reviewer(s) for their contribution to the peer review of this work. Primary Handling Editors: Clara Orbe and Clare Davis, Heike Langenberg, Alienor Lavergne. Peer reviewer reports are available.

**Reprints and permission information** is available at <http://www.nature.com/reprints>

**Publisher’s note** Springer Nature remains neutral with regard to jurisdictional claims in published maps and institutional affiliations.



**Open Access** This article is licensed under a Creative Commons Attribution 4.0 International License, which permits use, sharing, adaptation, distribution and reproduction in any medium or format, as long as you give appropriate credit to the original author(s) and the source, provide a link to the Creative Commons license, and indicate if changes were made. The images or other third party material in this article are included in the article’s Creative Commons license, unless indicated otherwise in a credit line to the material. If material is not included in the article’s Creative Commons license and your intended use is not permitted by statutory regulation or exceeds the permitted use, you will need to obtain permission directly from the copyright holder. To view a copy of this license, visit <http://creativecommons.org/licenses/by/4.0/>.

© The Author(s) 2022